



# Pt/C as a bifunctional ORR/iodide oxidation reaction (IOR) catalyst for Zn-air batteries with unprecedentedly high energy efficiency of 76.5%

Siyuan Zhao<sup>a</sup>, Tong Liu<sup>a,\*</sup>, Yawen Dai<sup>a</sup>, Jian Wang<sup>a,b</sup>, Yang Wang<sup>a</sup>, Zengjia Guo<sup>a</sup>, Jie Yu<sup>a</sup>, Idris Temitope Bello<sup>a</sup>, Meng Ni<sup>a,\*</sup>

<sup>a</sup> Building Energy Research Group, Department of Building and Real Estate, Research Institute for Sustainable Urban Development (RISUD) and Research Institute for Smart Energy (RISE), The Hong Kong Polytechnic University, Hung Hom, Kowloon, Hong Kong SAR, China

<sup>b</sup> School of Energy and Environment, City University of Hong Kong, Hong Kong SAR, China

## ARTICLE INFO

### Keywords:

Pt/C catalyst  
Charging voltage  
Energy efficiency  
Iodide oxidation  
Zn-air battery

## ABSTRACT

Rechargeable Zn-air batteries (ZABs) are promising for energy storage and conversion. However, the low energy efficiency caused by the high charging voltage greatly hinders their commercialization. Herein, potassium iodide (KI) is introduced to ZABs to change the oxidation pathway from the sluggish oxygen evolution reaction (OER) to  $\Gamma^-$  oxidation reaction (IOR) with faster kinetics and lower oxidation potential. Unexpectedly, the commercial carbon-based catalyst Pt/C with poor OER activity exhibits remarkable IOR activity. Benefitting from its high oxygen reduction reaction (ORR) activity, the fabricated ZABs deliver a low charging voltage of 1.68 V, high energy efficiency of 76.5%, and long cycle life of over 80 h at 5 mA cm<sup>-2</sup>. Density functional theory (DFT) calculation is conducted to reveal the IOR catalytic mechanism of the Pt/C catalyst. This work will reverse the traditional mindset on catalyst selection from ORR/OER to ORR/IOR and boost the commercialization of rechargeable ZABs.

## 1. Introduction

To meet the aim of carbon neutrality, developing sustainable and efficient energy conversion and storage technologies becomes more and more significant [1–4]. Nowadays, Li-ion batteries have occupied the market owing to their long lifetime and high energy density [5,6]. Nevertheless, they inevitably suffer from safety issues and limited Li reserves, which stimulate researchers to explore alternative energy technologies [7,8]. Aqueous rechargeable ZABs are promising candidates for their inherent safety, low cost, and high theoretical energy density (1084 Wh kg<sup>-1</sup>) [9–12]. Unfortunately, although with these advantages, ZABs have not been applied in practice yet. One of the critical issues hindering their commercialization is the low energy efficiency (~60%), which is mainly the result of high charging voltage (~2 V) [13–16]. Besides, the undesirable high charging voltage can degrade the cathode materials, resulting in shortened battery life [17]. Therefore, it is urgent to explore methods for lowering the charging voltage of ZABs.

OER takes place at the cathode side in charging process of ZABs. Regrettably, this process holds an intrinsically high thermodynamic

equilibrium voltage of 1.23 V [18]. Moreover, the kinetics of this process is sluggish due to the four electron-proton coupled transfer steps [19, 20]. These finally lead to ZAB's high charging voltage. Researchers have paid tremendous efforts to develop advanced catalysts for boosting the OER kinetics [21–25]. Besides, cathode optimizations from an engineering perspective, such as a compacted tri-electrode configuration, have been proposed to lower the battery charging voltage by accelerating electron transport [26]. However, the intrinsically sluggish OER pathway and high thermodynamic equilibrium voltage have set a firm ceiling for ZABs that most reported work cannot break through the charging voltage of ~1.9 V [27,28]. This stimulates researchers to think out of the box to substitute the formidable OER with other easily oxidized matters [29].

Recently, soluble potassium iodide (KI) has been proposed to act as a reaction modifier to help decrease the high charging voltage of ZABs [30,31]. This way, the sluggish OER pathway is replaced by the oxidation of  $\Gamma^-$  with accelerated kinetics and lower oxidation potential. However, the study is in the early stage that the whole  $\Gamma^-$  oxidation process has not been well understood yet and needs further exploration. Besides, the understanding of catalysts for ZABs with the KI reaction

\* Corresponding authors.

E-mail addresses: [tongliu@polyu.edu.hk](mailto:tongliu@polyu.edu.hk) (T. Liu), [meng.ni@polyu.edu.hk](mailto:meng.ni@polyu.edu.hk) (M. Ni).

<https://doi.org/10.1016/j.apcatb.2022.121992>

Received 9 March 2022; Received in revised form 7 August 2022; Accepted 14 September 2022

Available online 16 September 2022

0926-3373/© 2022 Elsevier B.V. All rights reserved.

modifier is insufficient. Although the OER pathway is altered, conventional OER catalysts are still employed in the previously reported works.

Herein, we demonstrate the whole IOR process in the alkaline environment is an electrochemical-chemical (E-C) process that  $I^-$  is first oxidized as  $I_2$ , which is unstable and then disproportion to  $I^-$  and  $IO_3^-$ . The replacement of OER by IOR is further confirmed by Raman and in situ microscopic. Besides, we find that poor OER performance may not indicate poor IOR performance: the commercial ORR catalyst Pt/C shows an undiscovered exceptional IOR activity, which facilitates the KI-modified ZABs to deliver an unprecedentedly low charging voltage of 1.68 V and high energy efficiency of 76.5% at 5 mA cm<sup>-2</sup>. In addition, since the cathode degradation is significantly alleviated, the battery obtains long cycle life of over 80 h. DFT calculation is further performed to reveal the remarkable IOR activity of the Pt/C catalyst. This work demonstrates the availability of IOR in narrowing ZABs' cycling overpotential, provides new insight into developing bifunctional ORR/IOR catalysts for high energy efficiency ZABs, and may boost future battery commercialization.

## 2. Experimental section

### 2.1. Materials

Potassium hydroxide (KOH, 90%, pellets), potassium iodide (KI, 99%, powder), potassium iodate (KIO<sub>3</sub>, 99.5%, powder), zinc acetate (Zn(Ac)<sub>2</sub>, 99%, powder), and iridium oxide (IrO<sub>2</sub>, 99.9% metals basis) are purchased from Macklin. 5 wt% Nafion solution is bought from Sigma-Aldrich. Carbon rod, Pt plate, carbon paper, Vulcan XC72 carbon, and 20% Pt/C catalyst are bought from Shanghai Hesen Corporation. Zn electrode (thickness of 0.2 mm) are purchased from Changsha Spring Corporation. Deionized water is used throughout the experiments. All the materials are used as received.

### 2.2. Electrolyte and working electrode preparation

#### 2.2.1. Oxygen evolution reaction (OER) testing

The electrolytes used for OER testing are 1 M KOH with 0 M, 0.167 M, 0.333 M, and 0.5 M KI. The working electrode Pt/C air cathode is prepared by the following process: 300 mg 20% Pt/C catalyst and 1 mL 5 wt% Nafion solution (binder) are first blended in a mortar with 20 mL ethanol. Then, this mixture is ground for 30 min to obtain a homogeneous ink. Finally, the homogeneous ink is stored in an airbrush and sprayed onto a 10 cm × 10 cm carbon papers with a mass loading of 1.5 mg cm<sup>-2</sup>. The preparation process of the working electrode IrO<sub>2</sub> air cathode is nearly the same as the Pt/C air cathode. The only difference is that 100 mg IrO<sub>2</sub> and 200 mg Vulcan XC72R carbon substitute the 300 mg 20% Pt/C.

#### 2.2.2. Oxygen reduction reaction (ORR) testing

The electrolytes used for ORR testing are 0.1 M KOH with 0 M, 0.0167 M, 0.0333 M, and 0.05 M KI. The working electrode for ORR testing is made by the following process: 0.47 mL isopropanol, 0.1 mL deionized water, 0.03 mL 5 wt% Nafion, and 5 mg Pt/C are first blended and sonicated for 30 min to attain a homogeneous ink. Then, 0.012 mL mixed ink is dropped on a 5 mm-diameter rotating disk electrode (RDE) and dried in the ambient until it is solidified. The mass loading is about 0.5 mg cm<sup>-2</sup>.

#### 2.2.3. Cyclic voltammetry (CV) testing

The electrolytes used for CV testing are 1 M KOH, 1 M KOH + 0.5 M KI, 1 M KOH + saturated KIO<sub>3</sub>, and 1 M KOH + 0.5 M KI + saturated KIO<sub>3</sub>. The used working electrode is a commercial 1 cm × 1 cm Pt plate.

#### 2.2.4. ZAB testing

The electrolytes for ZAB testing are 6 M KOH + 0.2 M Zn(Ac)<sub>2</sub> and 6 M KOH + 3 M KI + 0.2 M Zn(Ac)<sub>2</sub>. The used working electrode Pt/C air

cathode is the same in Section 2.2.1.

### 2.3. ZAB fabrication

The ZAB is assembled using a self-designed battery test model with the polished Zn plate as the anode, the sprayed Pt/C as the air cathode, and 6 M KOH + 0.2 M Zn(Ac)<sub>2</sub> or 6 M KOH + 3 M KI + 0.2 M Zn(Ac)<sub>2</sub> as the electrolytes (Fig. S1).

### 2.4. Electrolyte and air cathode characterization

Micro-Raman Spectroscopy System (Renishaw) is used to determine the charging product in the electrolyte. The applied voltage is 1.8 V, and the charging time is 2 h. A digital microscope (Sanqitid) is used to observe the oxygen evolution on the Pt/C air cathode during the battery charging process. Scanning electron microscope (SEM, HITACHI, S-4800) is used to observe the Pt/C air cathode. Transmission electron microscope (TEM, FEI Talos F200S) is used to observe the catalyst sonicated from the Pt/C air cathode. X-ray photoelectron spectroscopy (XPS, Thermo Scientific K-Alpha) is used to determine the oxidation states of C element and atomic ratio on the surface of the Pt/C air cathode.

### 2.5. Electrochemical performance and battery testing

All the electrochemical tests are conducted by Solartron in room temperature (25 °C). The OER and ORR performances are determined by linear sweep voltammetry (LSV) at a scanning rate of 5 mV s<sup>-1</sup>, where a Pt plate is the counter electrode, a Hg/HgO electrode is the reference electrode, and the catalyst loaded carbon paper (OER) and RDE (ORR, 1600 rpm) are the working electrode. CV measurements are conducted at different scan rates to reveal the transition process of  $I^-$ , where a Pt plate is the working electrode, a carbon rod is the counter electrode, and a Hg/HgO electrode is the reference electrode. All the electrodes are directly dipped in the working electrolyte mentioned in Section 2.2. The tested potentials versus Hg/HgO are transformed to the potentials vs. RHE by the equation:  $E_{RHE} = E_{Hg/HgO} + 0.059pH + 0.098$ . LSV with a scanning rate of 5 mV s<sup>-1</sup> is conducted to obtain ZABs' polarization profiles. Neware battery testing system is used to test ZABs' rate, discharge, and cycling performances.

### 2.6. Density functional theory calculation

Vienna Ab Initio Package (VASP) is employed to perform all the density functional theory (DFT) calculations within the generalized gradient approximation (GGA) using the PBE formulation [32–34]. We have chosen the projected augmented wave (PAW) potentials to describe the ionic cores and take valence electrons into account using a plane wave basis set with a kinetic energy cutoff of 450 eV [35,36]. Partial occupancies of the Kohn–Sham orbitals are allowed using the Gaussian smearing method with a width of 0.05 eV. The electronic energy is considered self-consistent when the energy change is smaller than 10<sup>-4</sup> eV. A geometry optimization is considered convergent when the force change is smaller than 0.03 eV/Å. Grimme's DFT-D3 methodology is used to describe the dispersion interactions [37]. The Brillouin zone integral uses the surface structures of 3 × 3 × 1 monkhorst pack K-point sampling. Finally, the adsorption energies ( $E_{ads}$ ) are calculated as  $E_{ads} = E_{ad/sub} - E_{ad} - E_{sub}$ , where  $E_{ad/sub}$ ,  $E_{ad}$ , and  $E_{sub}$  are the optimized adsorbate/substrate system, the adsorbate in the structure, and the clean substrate, respectively. The Gibbs free energy ( $\Delta G$ ) for the elemental reaction step is calculated as  $\Delta G = \Delta E + \Delta EZPE - T\Delta S$ , where  $\Delta E$  is the difference between the total energy,  $\Delta EZPE$  and  $\Delta S$  are the differences in the zero-point energy and the change of entropy, and  $T$  is the temperature ( $T = 300$  K in this work), respectively.

### 3. Results and discussion

#### 3.1. The substitution of OER by IOR

Commercial carbon-based ORR catalyst Pt/C has been widely used in the energy market due to its good quality and mature large-scale production technology [38,39]. However, their intrinsically poor OER activity determines them unsuitable for rechargeable ZABs [40]. As shown in Fig. 1a, the linear sweep voltammetry (LSV) curve of OER indicates that Pt/C catalyst as a working electrode delivers a high onset potential of 1.69 V (vs. RHE, same below) at  $10 \text{ mA cm}^{-2}$  in a three-electrode system with 1 M KOH. Besides, the Pt/C catalyst exhibits a high Tafel slope of  $138.5 \text{ mV dec}^{-1}$ , demonstrating the sluggish OER kinetics (Fig. 1b). Nevertheless, the values of these two evaluation indexes both

decline after introducing KI in the electrolyte, and the declining degree further gets enhanced with the increase in KI concentration. Finally, the Pt/C catalyst achieves 1.24 V and  $17.7 \text{ mV dec}^{-1}$  with half KI addition (Fig. 1a and b). This significant improvement in oxidation kinetics by poor OER catalysts indicates that the OER pathway is replaced by the oxidation of the  $\text{I}^-$  additive, which may intrinsically more readily be oxidized than hydroxide.

The oxidation product of  $\text{I}^-$  is most likely to be  $\text{IO}_3^-$  since other products like  $\text{I}_2$  are not stable in the alkaline environment. To further explore the IOR process and confirm the final product, in Fig. 1c, cyclic voltammetry (CV) scanning is conducted in KOH solution and that containing KI,  $\text{KIO}_3$ , and both. The strong anodic peak A within 1 and 2 V in KOH-KI solution represents the oxidation of  $\text{I}^-$ , while the strong cathodic peak C within 0 and 1 V in KOH- $\text{KIO}_3$  solution is attributed to

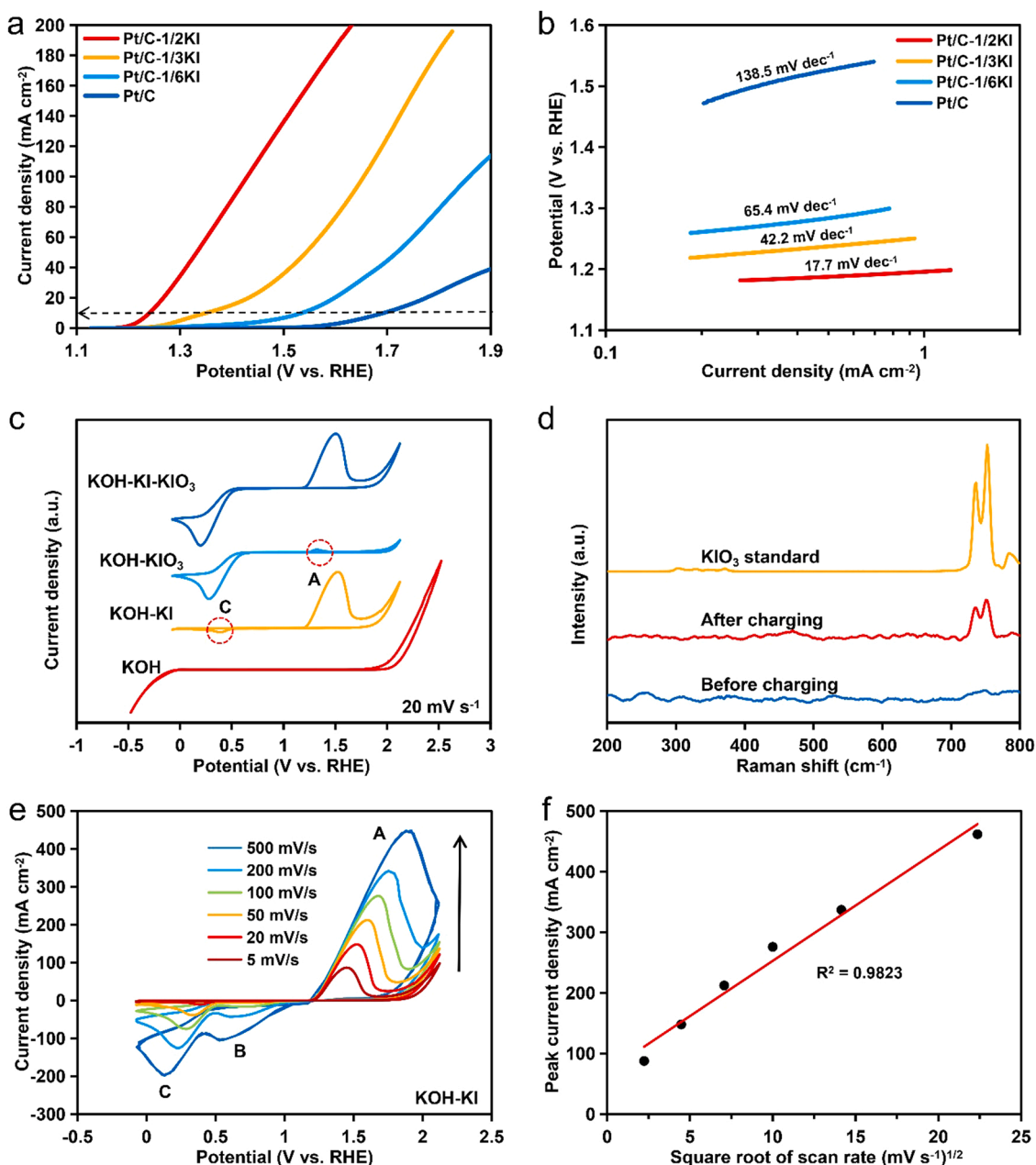


**Fig. 1.** (a) LSV curves of the Pt/C catalyst in 1 M KOH with 0, 1/6, 1/3, 1/2 M KI for OER (IOR) and (b) corresponding Tafel plots. (c) CV curves of the Pt foil in 1 M KOH, 1 M KOH + 0.5 M KI, 1 M KOH + saturated  $\text{KIO}_3$ , and 1 M KOH + 0.5 M KI + saturated  $\text{KIO}_3$  solutions at a scan rate of  $20 \text{ mV s}^{-1}$ . (d) Raman spectra of the precipitates from the battery electrolyte before and after charging and the pure  $\text{KIO}_3$  powders. (e) CV curves of the Pt foil in 1 M KOH + 0.5 M KI solution at various scan rates from 5 to  $500 \text{ mV s}^{-1}$ . (f) Relationship between the peak current density and the square root of scan rate.

the reduction of  $\text{IO}_3^-$ . Besides the strong peak, a weak cathodic peak C in KOH-KI solution is also observed, which corresponds well to the strong  $\text{IO}_3^-$  reduction peak C in KOH- $\text{KIO}_3$  solution. Moreover, apart from the peak A and C, no other peak is observed, demonstrating that the final oxidation product of  $\Gamma^-$  is  $\text{IO}_3^-$  [41]. By detecting the precipitated oxidation product with Micro-Raman, the peaks in the spectra are consistent with standard  $\text{KIO}_3$  powders (Fig. 1d), further confirming our conclusion from CV. In addition, the fact that anodic peak A in KOH-KI solution is much stronger than cathodic peak C also suggests the IOR pathway to  $\text{IO}_3^-$  is an E-C process [42]. That is, the  $\Gamma^-$  is first oxidized (electrochemical) to the intermediate  $\text{I}_2$ , which is unstable and then disproportionation (chemical) to  $\Gamma^-$  and  $\text{IO}_3^-$  in the alkaline environment. Besides, considering the significant improvement in Fig. 1a and b, the E-C process is reasonable because the kinetics of the two-electron pathway from  $\Gamma^-$  to  $\text{I}_2$  is far more rapid than the complicated direct six-electron pathway from  $\Gamma^-$  to  $\text{IO}_3^-$ . Unfortunately, the disproportionation of  $\text{I}_2$  is so swift that this process can only be observed at a higher CV scan rate. Therefore, in Fig. 1e, we gradually increase the scan rate from 5 to  $500 \text{ mV s}^{-1}$  in KOH-KI solution and peak B, which represents the reduction of  $\text{I}_2$  to  $\Gamma^-$ , becomes more and more distinct. The detection of peak B further approves the E-C process of IOR. Not only peak B, the peak current density of the  $\Gamma^-$  oxidation peak A also raises with the increase in scan rate (Fig. 1e). Moreover, the peak current density of the peak A and the corresponding square root of the scan rate exhibit a linear relationship (Fig. 1f), demonstrating the  $\Gamma^-$  oxidation is restricted by diffusion [43]. This finding explains why the oxidation performances in Fig. 1a and b get further improved when KI is more concentrated and supports ZABs' electrolyte design. The non-zero intercept on the fitting line indicates the non-faradaic current, which may be due to the electric double layer generated on the Pt working electrode [44,45].

Finally, we utilize an in-situ digital microscope to verify the IOR replacement on the Pt/C cathode of ZABs. An optimized electrolyte 6 M KOH + 3 M KI + 0.2 M  $\text{Zn}(\text{Ac})_2$  is employed (Fig. S2). When charging at a high current density of  $20 \text{ mA cm}^{-2}$ , no bubble is observed on the surface of the air cathode in the electrolyte with KI (Fig. 2a). By contrast, without KI, plenty of oxygen bubbles are immediately generated as soon as the voltage is applied (Fig. 2e). Besides, as time goes by, the air

cathode with KI remains still that no bubble is generated (Fig. 2a-d), while on the air cathode without KI, the continuously generated small bubbles gradually accumulate to become larger bubbles (Fig. 2e-h). Since IOR is a no-bubble-generation reaction and the OER is a bubble-generation reaction, the above comparison provides strong support that the IOR substitutes the OER pathway. Moreover, catalysts on the air cathode detach into the electrolyte (circled by the red dash line in Fig. 2g and h) along with the detachment of oxygen bubbles, which may cause performance deterioration.

On the other hand, according to the previous research, the reduction of  $\text{IO}_3^-$  on the cathode can be neglected when oxygen is sufficient, indicating that the cathodic reaction during the discharge process of ZABs remains ORR [41]. Therefore, the overall reaction of ZABs with the KI

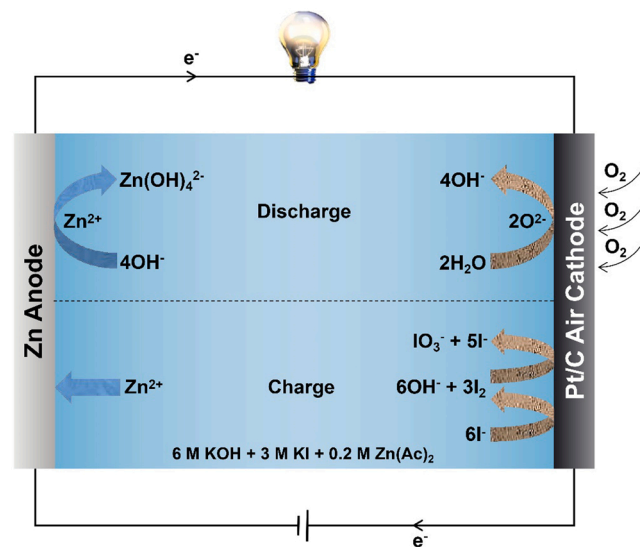


Fig. 3. Schematic of the reactions within ZABs with KI additive during charging and discharge process.

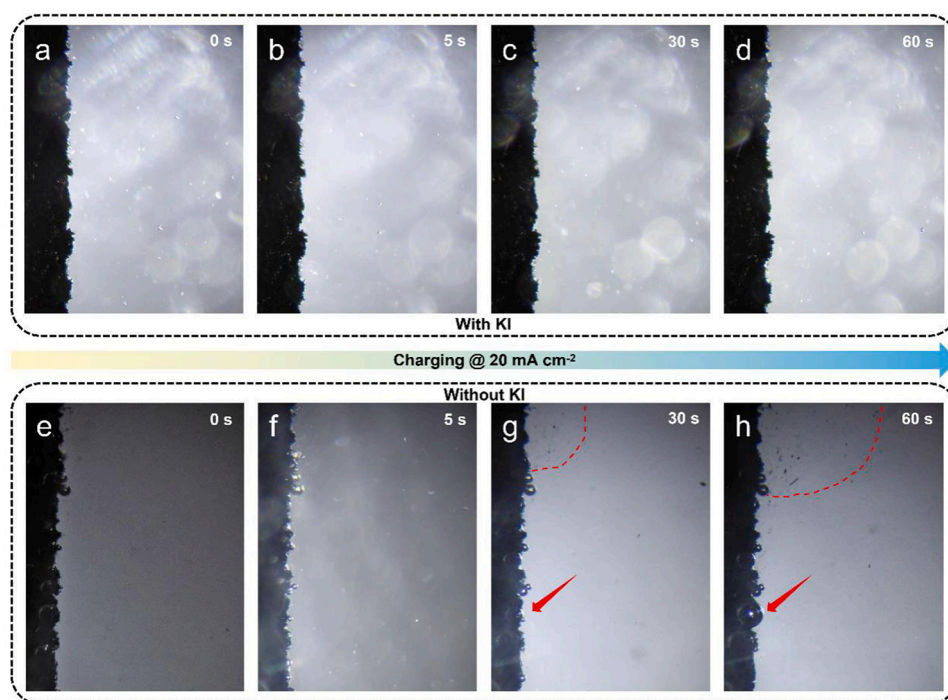


Fig. 2. During  $20 \text{ mA cm}^{-2}$  charging process, in-situ microscopic section images of the Pt/C air cathode's surface in 6 M KOH + 0.2 M  $\text{Zn}(\text{Ac})_2$  electrolyte (a)-(d) with and (e)-(h) without 3 M KI.



modifier can be summarized in Fig. 3. During battery discharge, Zn dissolves in the alkaline electrolyte and transfers to  $\text{Zn(OH)}_4^{2-}$ , while the air cathode adsorbs the oxygen from the ambient and reduces it into  $\text{OH}^-$  [46]. During the charging process, Zn ions deposit on the anode, and  $\text{I}^-$  is first oxidized to  $\text{I}_2$ , followed by disproportionation to  $\text{I}^-$  and  $\text{IO}_3^-$  on the cathode. Since the hydrogen evolution reaction (HER) on the Zn surface is weak in an alkaline environment and will hardly affect the battery performance, it is not discussed in this work. However, at a higher charging voltage, the HER kinetics should be considered.

### 3.2. Mechanism for the superior IOR performance of Pt/C

Since the ORR is retained and the IOR replaces the sluggish OER pathway, the bifunctional catalyst selection for the KI-modified ZABs should be transformed from conventional ORR/OER to ORR/IOR catalysts. However, because the study on this KI-modified system is in its infancy, researchers haven't realized the altered IOR pathway that they are still using ORR/OER catalysts, such as Pt/C- $\text{Co}_3\text{O}_4$  and Pt/C- $\text{RuO}_2$  [30,31]. Here, we want to clarify that the OER electrocatalytic activity is not equal to IOR. As shown in Fig. 4a, although the Pt/C catalyst exhibits expectedly worse OER activity than the OER benchmark  $\text{IrO}_2$  catalyst, its onset potential is lower when KI exists, demonstrating a superior IOR

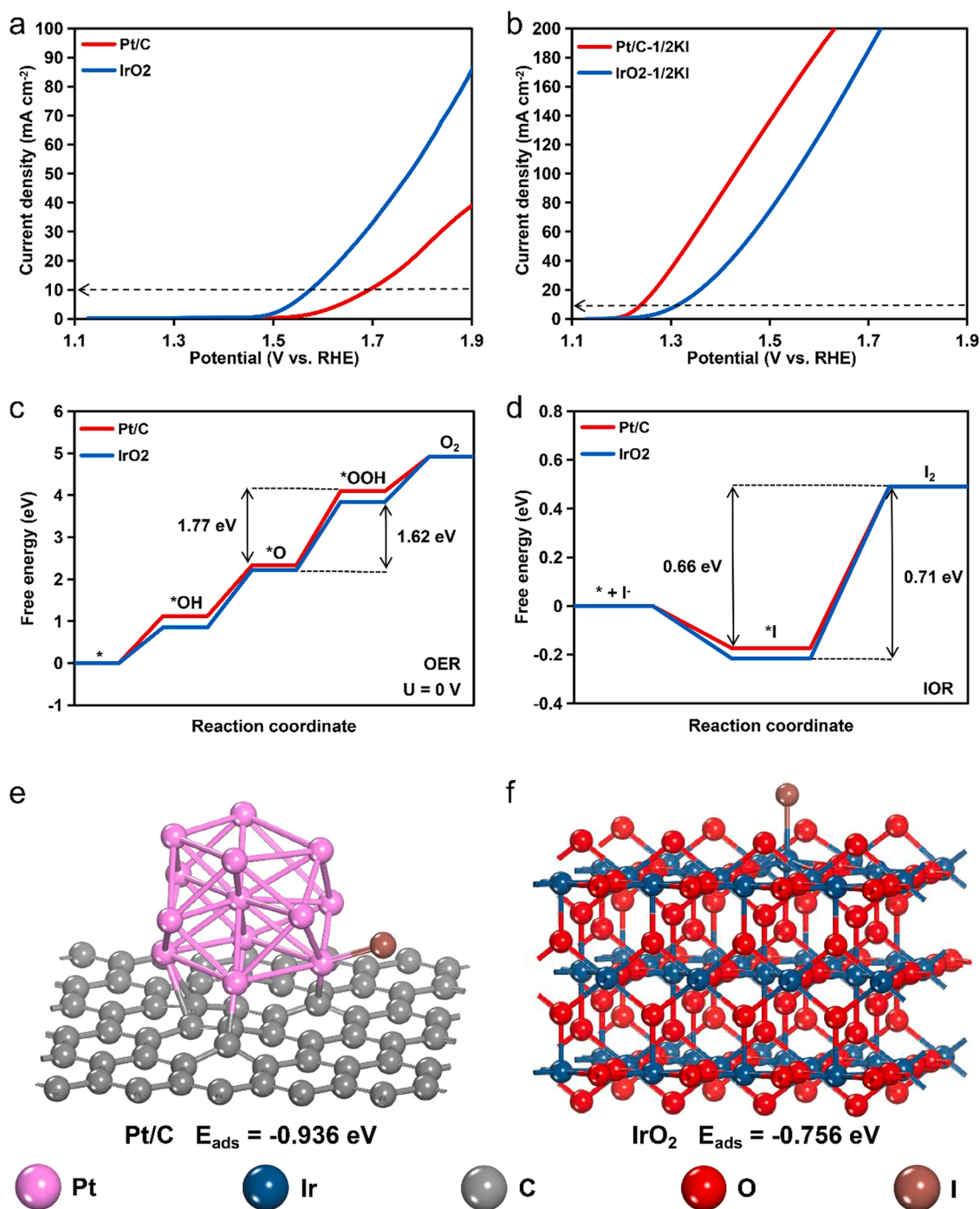


**Fig. 4.** (a) LSV curves of the Pt/C and  $\text{IrO}_2$  catalysts in 1 M KOH for OER and (b) 1 M KOH + 1/2 M KI for IOR. (c) OER free energy diagrams of the Pt/C and  $\text{IrO}_2$  catalysts at 0 V. (d) IOR free energy diagrams of the Pt/C and  $\text{IrO}_2$  catalysts. Adsorption models of the (e) Pt/C and (f)  $\text{IrO}_2$  catalysts and their corresponding  $E_{\text{ads}}$ .

performance (Fig. 4b). The above results further demonstrate that the mindset for catalyst selection should be rebuilt and not follow the one for ORR/OER. To obtain a deeper understanding of the differences between OER and IOR, density functional theory (DFT) calculation is performed to reveal the mechanism of the lower onset potential of IOR and the higher IOR activity of Pt/C. First, Pt/C and IrO<sub>2</sub> models are constructed in Fig. S3 to present the oxygen intermediates during the OER process. As shown in Fig. 4c, the Gibbs free energy change ( $\Delta G$ ) of the rate-determining step from  $\ast\text{O} \rightarrow \ast\text{OOH}$  ( $\ast$  denotes the active site) of the IrO<sub>2</sub> catalyst (1.62 eV) is lower than that of the Pt/C catalyst (1.77 eV), demonstrating a lower energy barrier, which is consistent with the result in Fig. 4a. When OER is replaced by IOR, the rate-determining step is also altered from  $\ast\text{O} \rightarrow \ast\text{OOH}$  to  $\ast\text{I} \rightarrow \text{I}_2$ , where the  $\Delta G$  of the Pt/C catalyst is 0.66 eV, and the IrO<sub>2</sub> catalyst is 0.71 eV, both of which are significantly lower than that in the OER process (Fig. 4d, with  $\Gamma$  adsorption models in Fig. 4e and f). In addition, the  $\Gamma$  adsorption energies ( $E_{\text{ads}}$ ) of the Pt/C and IrO<sub>2</sub> are both negative, indicating the  $\Gamma$  adsorption processes are thermodynamically favorable. Moreover, the Pt/C catalyst exhibits a stronger interaction with  $\Gamma$  with the lower  $E_{\text{ads}}$  of  $-0.936$  eV than the IrO<sub>2</sub> catalyst. The lower IOR  $\Delta G$  and  $E_{\text{ads}}$  of the Pt/C catalyst further explain the outperformed electrocatalytic activity in Fig. 4b. The above analysis shows that although the Pt/C catalyst is not as favorable as the IrO<sub>2</sub> catalyst to catalyze OER, it has exhibited stronger interaction with  $\Gamma$  and better IOR performance. Therefore, we can believe in the previous reports that the catalyst that works is Pt, while the RuO<sub>2</sub> and Co<sub>3</sub>O<sub>4</sub> may be redundant. Since the Pt/C catalyst is also known as a good ORR catalyst, it is qualified to serve as a bifunctional catalyst for KI-modified rechargeable ZABs.

### 3.3. Electrochemical performance of ZAB

A series of battery testing is conducted to further investigate the effect of KI and the commercial Pt/C catalyst on ZABs [47]. As the shown charging polarization profiles in Fig. 5a, the Pt/C based ZAB with the KI modifier delivers a significantly lower charging voltage than the conventional one without KI. Even at a current density of  $100 \text{ mA cm}^{-2}$ , the charging voltage is still under 2 V. For the discharge polarization process, the adding of KI will slightly decrease the battery discharge voltage, which may be due to the partly occupying of ORR active sites by  $\Gamma$ . The ORR LSV profiles also show the corresponding performance decline (Fig. S4). Fortunately, the voltage decrease in discharge voltage is not distinct, and the KI-modified ZAB is still at the same high level as the conventional ZAB. Besides, ZABs with the KI modifier exhibit a notably high peak power density of  $148.8 \text{ mW cm}^{-2}$ , very close to the benchmark ORR performance by Pt/C without KI (Fig. 5b). The battery rate performances under various current densities from 1 to  $50 \text{ mA cm}^{-2}$  are also provided in Fig. 5c. The KI-modified ZAB shows a much narrower voltage gap because of the decreased charging voltage and the hardly affected high discharge voltage. Besides, it promptly reaches a stable voltage platform of  $\sim 1.63 \text{ V}$  when charging starts, but it takes longer for conventional ZABs. Moreover, the charging voltage of ZABs with KI can maintain as low as  $\sim 1.91 \text{ V}$  and high stability even at  $50 \text{ mA cm}^{-2}$ , while that of the conventional ZABs shows  $\sim 2.22 \text{ V}$  and a rising tendency. These improvements are attributed to KI and the outstanding bifunctional ORR/IOR Pt/C catalyst. ZABs with and without KI also display stable discharge voltages of  $\sim 1.31 \text{ V}$  and high specific capacities of  $\sim 800 \text{ mAh g}^{-1}$  at  $5 \text{ mA cm}^{-2}$  (Fig. 5d). When the current density increases to  $10 \text{ mA cm}^{-2}$ , the battery discharge performance is still very satisfactory (Fig. S5). The slight voltage decrease is mainly due to the Zn consumption and morphology change during the discharging process (Fig. S6).

Finally, we evaluate the rechargeability and cycling stability of the Pt/C based ZABs at  $5 \text{ mA cm}^{-2}$ . As shown in Fig. 5e, although the ZAB without KI shows a slightly higher discharge voltage than that without KI, the battery charging voltage soon rises to 2.5 V after several cycles, leading to quick battery failure. On the other hand, by virtue of the

intrinsically readily  $\Gamma$  oxidation pathway and the remarkable bifunctional ORR/IOR catalytic activity of Pt/C catalyst, the KI-modified ZAB exhibits a significantly decreased charging voltage of 1.68 V and unprecedentedly high energy efficiency of 76.5% at  $5 \text{ mA cm}^{-2}$ , surpassing all the reported metal-based or metal-free catalysts with complicated synthesis steps and low yields (Fig. 5f) [48–54]. Moreover, compared to other ZABs with reaction modifiers, the presented KI-modified ZAB also shows superior performances (Table S2) [30, 55–58]. Furthermore, at 20 min per cycle, the KI-modified ZAB's cycle life is considerably extended to over 80 h, about 10 times the conventional ZABs. The energy efficiency can also retain 70.6% after 240 cycles, demonstrating exceptional cycling stability. We then perform the OER/IOR activity testing of the above two used Pt/C cathodes. As shown in Fig. S7, the onset potential of the cathode with KI hardly changes compared to its initial state, while that of the other one without KI is distinctly higher. The ZAB's charging stability tests also demonstrate that the existence of KI can significantly alleviate the performance degradation of the Pt/C catalyst (Fig. S8). The main electrochemical performances have been repeated for three times and obtained consistent results, demonstrating the reproducibility of the presented strategy (Fig. S9). Moreover, We also notice that the color of the electrolyte without KI changes from transparent to deep brown, indicating severe carbon corrosion and catalyst detachment on the air cathode under a higher charging voltage (inset in Fig. 5e) [59]. However, the electrolyte with KI remains transparent after cycling, demonstrating the oxygen bubble-free IOR process with lower charging potential can protect the air cathode well and endow the battery with a longer lifetime. For practical applications such as large-scale energy storage and conversion, it is required the battery can work for a long period. Therefore, we extend the battery cycle period to 2 h. As shown in Fig. 5g, Pt/C based ZABs with KI exhibit very stable charging and discharging voltage and unaffected lifetime. Moreover, the battery can maintain a stable open circuit voltage (OCV) for over 10 days, demonstrating a good shelf-life (Fig. S10). Further beneficial from Pt/C's mature large-scale production technology, the presented ZABs will have great potential in future practical applications. The strategy of using Pt/C and KI is also applicable for flexible ZABs with absorbent polymer electrolytes, which may boost the development of flexible electronic devices [12,16].

### 3.4. Characterization of the cycled Pt/C air cathode and Zn anode

To further investigate the effect of KI in extending battery cycle life, XPS, TEM and SEM are conducted on the Pt/C air cathode because its degradation is the reason for battery failure. From the C 1 s XPS spectra of the initial Pt/C catalyst, only a C-C bond at 284.8 eV and a broad C-O bond at  $\sim 286 \text{ eV}$  are observed (Fig. 6a). After cycling for 80 h in the electrolyte with KI, the Pt/C catalyst shows no distinct difference to the pristine one, demonstrating the surface carbon in Pt/C is well protected under a lower charging voltage (Fig. 6b). However, for the Pt/C catalyst of the failed battery without KI, a new C=O peak at  $\sim 288.5 \text{ eV}$  shows up, and the broad C-O peak becomes sharper and higher, indicating the more severe carbon corrosion (oxidation) at a higher charging voltage (Fig. 6c) [60]. The atomic ratio of the Pt/C catalyst can further prove the protection by the lower voltage. As shown in Fig. 6d and e, without KI, the O atomic ratio and the content of C-O and C=O bond on the Pt/C's surface increase obviously after battery cycling. Besides, the Pt atomic ratio declines significantly due to its dissolution and the oxidation of the supported carbon in Pt/C at a higher voltage (Fig. 6e) [61]. The decline can be further reflected by the weakened Pt intensity in Fig. S11. The continuously generated oxygen bubbles during battery charging process (Fig. 2e-h) will also lead to the Pt detachment. Since adding KI can lower charging voltage and avoid bubble generation, the Pt content remains close to its pristine state, and carbon corrosion is remarkably mitigated. Finally, KI-modified ZABs with the Pt/C catalyst show extended cycle life.

The TEM images are also consistent with the XPS results above. As

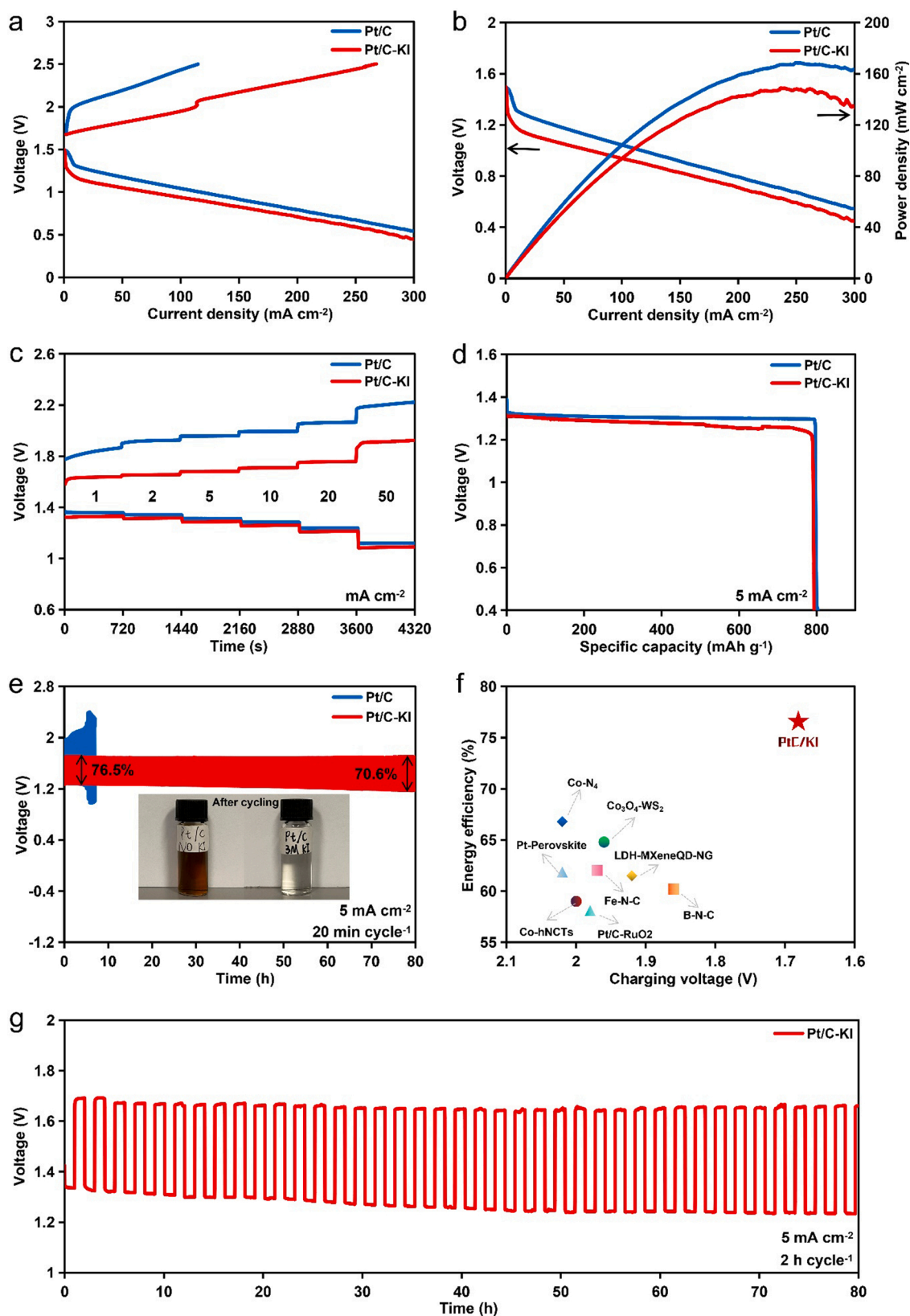


**Fig. 5.** Electrochemical performances of the Pt/C catalyst based ZABs with and without KI. (a) Charge and discharge polarization profiles. (b) Discharge polarization profiles and the corresponding power density curves. (c) Charge and discharge rate performances. (d) Discharge specific capacity profiles at 5  $\text{mA cm}^{-2}$ . (e) Galvanostatic charge and discharge cycle performances at 5  $\text{mA cm}^{-2}$  and 20 min per cycle. The inset shows the color change of the electrolytes after cycling. (f) Energy efficiency and charging voltage comparison of ZABs with various catalysts at 5  $\text{mA cm}^{-2}$ . (g) Galvanostatic charge and discharge cycle performances at 5  $\text{mA cm}^{-2}$  and 2 h per cycle.



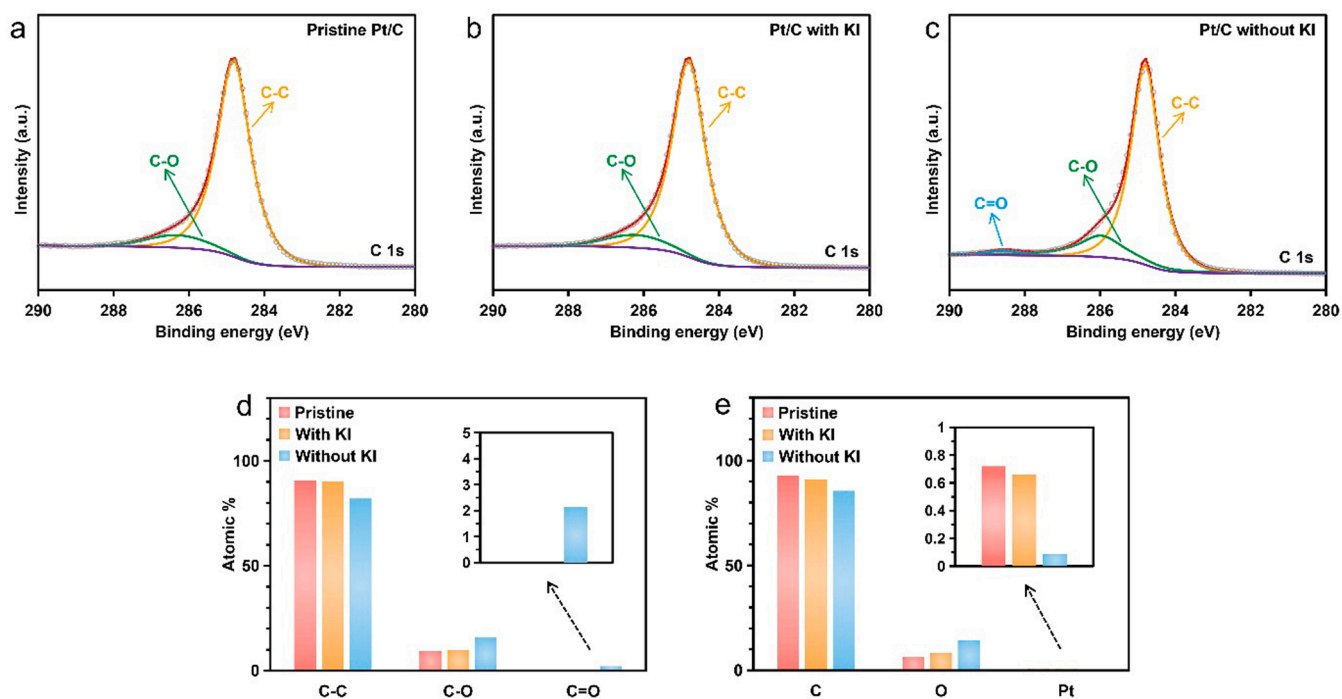


**Fig. 6.** C 1s XPS spectra of the Pt/C catalyst (a) before and after battery cycling (b) with and (c) without KI. The corresponding (d) fitted C 1s and (e) overall atomic ratio.

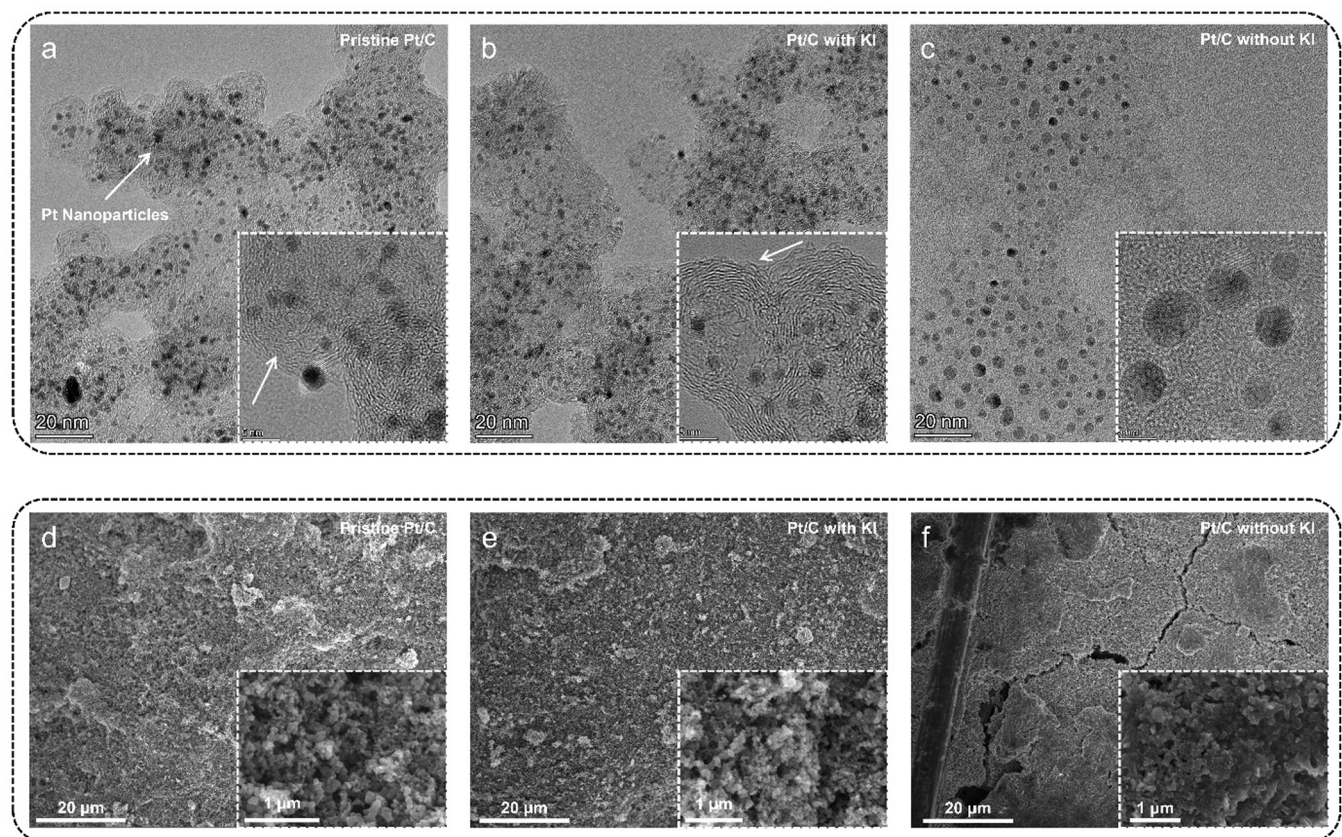


**Fig. 7.** The effect of KI on the Pt/C catalyst' morphology and structure. (a)-(c) TEM images and HRTEM insets of the Pt/C catalyst before and after battery cycling. Scale bar: 20 nm and 5 nm (inset). (d)-(f) SEM images of the Pt/C catalyst before after battery cycling. Scale bar: 20  $\mu\text{m}$  and 1  $\mu\text{m}$  (inset).



shown in Fig. 7a, Pt nanoparticles of the pristine Pt/C catalyst disperse uniformly and densely, and the supported carbon also exhibits a distinct onion-like morphology. After repeating ORR/IOR cycles lasting 80 h, the Pt concentration hardly changed, and the onion-like morphology remains, indicating a well preserved high catalytic performance (Fig. 7b) [62]. However, after battery failure without KI, the Pt nanoparticles are sparse, and the supported carbon becomes vague (Fig. 7c). This phenomenon demonstrates the extreme cathode corrosion at a higher charging voltage [63,64]. Besides, the size of the Pt nanoparticles gets larger, leading to a decreased electrochemically active surface area [65]. These degradations explain the rapid battery failure in Fig. 5e. We also provide SEM images to depict the cathode morphology change. Referring to the initial Pt/C air cathode in Fig. 7d, the cathode in the electrolyte with KI can maintain intact after 80-hour battery cycling (Fig. 7e). Nevertheless, the one without KI cracks due to the continuous impulse by the generated oxygen bubbles (Fig. 7f) [26]. Moreover, as shown in Fig. 7e inset with higher magnification, the nanoparticles on the air cathode retain well dispersed after cycling with KI. However, they agglomerate in the electrolyte without KI (Fig. 7f), consistent with the TEM result in Fig. 7c. Apart from the air cathode, the reduced charging voltage can also alleviate the Zn dendrite problem. As shown in Fig. S12, the surface morphology of the Zn plate shows larger Zn particles and nonuniform Zn plating after continuous cycles without KI. In contrast, the one with KI is flatter and denser, demonstrating the advantage of KI in inducing uniform Zn plating.

#### 4. Conclusion

In summary, we introduce a reaction modifier KI to ZABs for lowering the battery charging voltage and confirm the I<sup>−</sup> oxidation process and its replacement of the conventional OER pathway. Moreover, commercial carbon-based catalyst Pt/C have been developed as a bifunctional ORR/IOR catalyst for rechargeable ZABs, which deliver a low charging voltage of 1.68 V, high energy efficiency of 76.5%, and long cycle life of over 80 h at 5 mA cm<sup>−2</sup>. Further DFT calculation is also conducted to reveal the I<sup>−</sup> oxidation mechanism by the Pt/C catalyst. It is believed this work can provide a novel insight into developing bifunctional ORR/IOR catalysts and further boost the future commercialization of ZABs.

#### CRedit authorship contribution statement

**Siyan Zhao:** Conceptualization, Methodology, Investigation, Writing – original draft. **Tong Liu:** Investigation, Writing – review & editing, Supervision. **Yawen Dai:** Investigation, Validation. **Jian Wang:** Investigation, Validation. **Yang Wang:** Validation. **Zengjia Guo:** Investigation. **Jie Yu:** Validation. **Idris Temitope Bello:** Validation. **Meng Ni:** Conceptualization, Funding acquisition, Writing – review & editing, Supervision, Project administration.

#### Declaration of Competing Interest

The authors declare that they have no known competing financial interests or personal relationships that could have appeared to influence the work reported in this paper.

#### Data availability

Data will be made available on request.

#### Acknowledgments

This work is supported by a grant from Collaborative Research Fund (CRF) (Project no. C5031-20G) of Research Grants Council, University Grants Committee, HK SAR, and Guangdong Basic and Applied Basic Research Foundation (2021A1515110464).

#### Appendix A. Supplementary material

Supplementary data associated with this article can be found in the online version at doi:10.1016/j.apcatb.2022.121992.

#### References

- [1] P. Tan, B. Chen, H. Xu, H. Zhang, W. Cai, M. Ni, M. Liu, Z. Shao, Flexible Zn–air batteries: recent advances, challenges, and future perspectives, *Energy Environ. Sci.* 10 (10) (2017) 2056–2080, <https://doi.org/10.1039/C7EE01913K>.
- [2] H. Li, L. Ma, C. Han, Z. Wang, Z. Liu, Z. Tang, C. Zhi, Advanced rechargeable zinc-based batteries: Recent progress and future perspectives, *Nano Energy* 62 (2019) 550–587, <https://doi.org/10.1016/j.nanoen.2019.05.059>.
- [3] H. Chen, X. Zhang, S. Wu, F. Chen, J. Xu, A comparative study of iron-vanadium and all-vanadium flow battery for large scale energy storage, *Chem. Eng. J.* 429 (2022), 132403, <https://doi.org/10.1016/j.cej.2021.132403>.
- [4] Y. Yang, E.G. Okonkwo, G. Huang, S. Xu, W. Sun, Y. He, On the sustainability of lithium ion battery industry—a review and perspective, *Energy Storage Mater.* 36 (2021) 186–212, <https://doi.org/10.1016/j.ensm.2020.12.019>.
- [5] J.B. Goodenough, How we made the Li-ion rechargeable battery, 204–204, *Nat. Electron.* 1 (3) (2018), <https://doi.org/10.1038/s41928-018-0048-6>.
- [6] J. Xie, Y.-C. Lu, A retrospective on lithium-ion batteries, *Nat. Commun.* 11 (1) (2020) 1–4, <https://doi.org/10.1038/s41467-020-16259-9>.
- [7] Y. Chen, Y. Kang, Y. Zhao, L. Wang, J. Liu, Y. Li, Z. Liang, X. He, X. Li, N. Tavajohi, A review of lithium-ion battery safety concerns: the issues, strategies, and testing standards, *J. Energy Chem.* 59 (2021) 83–99, <https://doi.org/10.1016/j.jechem.2020.10.017>.
- [8] S. Zhao, Y. Zuo, T. Liu, S. Zhai, Y. Dai, Z. Guo, Y. Wang, Q. He, L. Xia, C. Zhi, Multifunctional hydrogels for flexible zinc-based batteries working under extreme conditions, *Adv. Energy Mater.* 11 (34) (2021) 2101749, <https://doi.org/10.1002/aenm.202101749>.
- [9] S. Zhao, K. Wang, S. Tang, X. Liu, K. Peng, Y. Xiao, Y. Chen, A new solid-state zinc–air battery for fast charge, *Energy Technol.* 8 (5) (2020) 1901229, <https://doi.org/10.1002/ente.201901229>.
- [10] W. Shang, W. Yu, Y. Liu, R. Li, Y. Dai, C. Cheng, P. Tan, M. Ni, Rechargeable alkaline zinc batteries: Progress and challenges, *Energy Storage Mater.* 31 (2020) 44–57, <https://doi.org/10.1016/j.ensm.2020.05.028>.
- [11] X. Zhong, S. Ye, J. Tang, Y. Zhu, D. Wu, M. Gu, H. Pan, B. Xu, Engineering Pt and Fe dual-metal single atoms anchored on nitrogen-doped carbon with high activity and durability towards oxygen reduction reaction for zinc–air battery, *Appl. Catal. B Environ.* 286 (2021), 119891, <https://doi.org/10.1016/j.apcatb.2021.119891>.
- [12] S. Ramakrishnan, D.B. Velusamy, S. Sengodan, G. Nagaraju, D.H. Kim, A.R. Kim, D. J. Yoo, Rational design of multifunctional electrocatalyst: an approach towards efficient overall water splitting and rechargeable flexible solid-state zinc–air battery, *Appl. Catal. B Environ.* 300 (2022), 120752, <https://doi.org/10.1016/j.apcatb.2021.120752>.
- [13] Y. Li, M. Gong, Y. Liang, J. Feng, J.-E. Kim, H. Wang, G. Hong, B. Zhang, H. Dai, Advanced zinc–air batteries based on high-performance hybrid electrocatalysts, *Nat. Commun.* 4 (1) (2013) 1–7, <https://doi.org/10.1038/ncomms2812>.
- [14] Y.-P. Deng, Y. Jiang, R. Liang, S.-J. Zhang, D. Luo, Y. Hu, X. Wang, J.-T. Li, A. Yu, Z. Chen, Dynamic electrocatalyst with current-driven oxyhydroxide shell for rechargeable zinc–air battery, *Nat. Commun.* 11 (1) (2020) 1–10, <https://doi.org/10.1038/s41467-020-15853-1>.
- [15] C. Lai, J. Fang, X. Liu, M. Gong, T. Zhao, T. Shen, K. Wang, K. Jiang, D. Wang, In situ coupling of NiFe nanoparticles with N-doped carbon nanofibers for Zn–air batteries driven water splitting, *Appl. Catal. B Environ.* 285 (2021), 119856, <https://doi.org/10.1016/j.apcatb.2020.119856>.
- [16] E. Vijayakumar, S. Ramakrishnan, C. Sathiskumar, D.J. Yoo, J. Balamurugan, H. S. Noh, D. Kwon, Y.H. Kim, H. Lee, MOF-derived CoP-nitrogen-doped carbon@NiFeP nanoflakes as an efficient and durable electrocatalyst with multiple catalytically active sites for OER, HER, ORR and rechargeable zinc–air batteries, *Chem. Eng. J.* 428 (2022), 131115, <https://doi.org/10.1016/j.cej.2021.131115>.
- [17] T. Liu, S. Zhao, Y. Wang, J. Yu, Y. Dai, J. Wang, X. Sun, K. Liu, M. Ni, In situ anchoring Co–N–C nanoparticles on Co4N nanosheets toward ultrastable flexible self-supported bifunctional oxygen electrocatalyst enables recyclable Zn–air batteries over 10 000 cycles and fast charging, *Small* (2021) 2105887, <https://doi.org/10.1002/sml.202105887>.
- [18] Q. Xu, J. Zhang, H. Zhang, L. Zhang, L. Chen, Y. Hu, H. Jiang, C. Li, Atomic heterointerface engineering overcomes the activity limitation of electrocatalysts and promises highly-efficient alkaline water splitting, *Energy Environ. Sci.* 14 (10) (2021) 5228–5259, <https://doi.org/10.1039/D1EE02105B>.
- [19] X. Liu, Y. Yuan, J. Liu, B. Liu, X. Chen, J. Ding, X. Han, Y. Deng, C. Zhong, W. Hu, Utilizing solar energy to improve the oxygen evolution reaction kinetics in zinc–air battery, *Nat. Commun.* 10 (1) (2019) 1–10, <https://doi.org/10.1038/s41467-019-12627-2>.
- [20] H. Sun, W. Zhang, J.-G. Li, Z. Li, X. Ao, K.-H. Xue, K.K. Ostrikov, J. Tang, C. Wang, Rh-engineered ultrathin NiFe-LDH nanosheets enable highly-efficient overall water splitting and urea electrolysis, *Appl. Catal. B Environ.* 284 (2021), 119740, <https://doi.org/10.1016/j.apcatb.2020.119740>.
- [21] J. Song, C. Wei, Z.-F. Huang, C. Liu, L. Zeng, X. Wang, Z.J. Xu, A review on fundamentals for designing oxygen evolution electrocatalysts, *Chem. Soc. Rev.* 49 (7) (2020) 2196–2214, <https://doi.org/10.1039/C9CS00607A>.

- [22] Y. Dai, J. Yu, C. Cheng, P. Tan, M. Ni, Mini-review of perovskite oxides as oxygen electrocatalysts for rechargeable zinc-air batteries, *Chem. Eng. J.* 397 (2020), 125516, <https://doi.org/10.1016/j.cej.2020.125516>.
- [23] A. Saad, D. Liu, Y. Wu, Z. Song, Y. Li, T. Najam, K. Zong, P. Tsiakaras, X. Cai, Ag nanoparticles modified crumpled borophene supported Co<sub>3</sub>O<sub>4</sub> catalyst showing superior oxygen evolution reaction (OER) performance, *Appl. Catal. B Environ.* 298 (2021), 120529, <https://doi.org/10.1016/j.apcatb.2021.120529>.
- [24] H. Li, J. Wang, R. Qi, Y. Hu, J. Zhang, H. Zhao, J. Zhang, Y. Zhao, Enhanced Fe 3d delocalization and moderate spin polarization in FeNi atomic pairs for bifunctional ORR and OER electrocatalysis, *Appl. Catal. B Environ.* 285 (2021), 119778, <https://doi.org/10.1016/j.apcatb.2020.119778>.
- [25] S. Ramakrishnan, J. Balamurugan, M. Vinothkannan, A.R. Kim, S. Sengodan, D. J. Yoo, Nitrogen-doped graphene encapsulated FeCoMoS nanoparticles as advanced trifunctional catalyst for water splitting devices and zinc-air batteries, *Appl. Catal. B Environ.* 279 (2020), 119381, <https://doi.org/10.1016/j.apcatb.2020.119381>.
- [26] X. Li, Y. Tang, H. Lv, W. Wang, F. Mo, G. Liang, C. Zhi, H. Li, Recent advances in flexible aqueous zinc-based rechargeable batteries, *Nanoscale* 11 (39) (2019) 17992–18008, <https://doi.org/10.1039/c9nr06721c>.
- [27] L. Ye, Y. Hong, M. Liao, B. Wang, D. Wei, H. Peng, L. Ye, Y. Hong, M. Liao, B. Wang, D. Wei, H. Peng, Recent advances in flexible fiber-shaped metal-air batteries, *Energy Storage Mater.* 28 (2020) 364–374, <https://doi.org/10.1016/j.ensm.2020.03.015>.
- [28] M. Luo, W. Sun, B.B. Xu, H. Pan, Y. Jiang, Interface engineering of air electrocatalysts for rechargeable zinc-air batteries, *Adv. Energy Mater.* 11 (4) (2021) 2002762, <https://doi.org/10.1002/aenm.202002762>.
- [29] Z.-Y. Yu, C.-C. Lang, M.-R. Gao, Y. Chen, Q.-Q. Fu, Y. Duan, S.-H. Yu, Ni–Mo–O nanorod-derived composite catalysts for efficient alkaline water-to-hydrogen conversion via urea electrolysis, *Energy Environ. Sci.* 11 (7) (2018) 1890–1897, <https://doi.org/10.1039/C8EE00521D>.
- [30] Z. Song, J. Ding, B. Liu, X. Liu, X. Han, Y. Deng, W. Hu, C. Zhong, A rechargeable Zn-air battery with high energy efficiency and long life enabled by a highly water-retentive gel electrolyte with reaction modifier, *Adv. Mater.* 32 (22) (2020) 1908127, <https://doi.org/10.1002/adma.201908127>.
- [31] Y. Zhang, Y. Chen, X. Li, M. Alfred, D. Li, F. Huang, Q. Wei, Bacterial cellulose hydrogel: a promising electrolyte for flexible zinc-air batteries, *J. Power Sources* 482 (2021), 228963, <https://doi.org/10.1016/j.jpowsour.2020.228963>.
- [32] G. Kresse, J. Furthmüller, Efficient iterative schemes for ab initio total-energy calculations using a plane-wave basis set, *Phys. Rev. B* 54 (16) (1996) 11169, <https://doi.org/10.1103/PhysRevB.54.11169>.
- [33] J.P. Perdew, K. Burke, M. Ernzerhof, Generalized gradient approximation made simple, *Phys. Rev. Lett.* 77 (18) (1996) 3865, <https://doi.org/10.1103/PhysRevLett.77.3865>.
- [34] G. Kresse, D. Joubert, From ultrasoft pseudopotentials to the projector augmented-wave method, *Phys. Rev. B* 59 (3) (1999) 1758, <https://doi.org/10.1103/PhysRevB.59.1758>.
- [35] P.E. Blöchl, Projector augmented-wave method, *Phys. Rev. B* 50 (24) (1994) 17953, <https://doi.org/10.1103/PhysRevB.50.17953>.
- [36] S. Grimme, J. Antony, S. Ehrlich, H. Krieg, A consistent and accurate ab initio parametrization of density functional dispersion correction (DFT-D) for the 94 elements H–Pu, *J. Chem. Phys.* 132 (15) (2010), 154104, <https://doi.org/10.1063/1.3382344>.
- [37] G. Henkelman, B.P. Uberuaga, H. Jónsson, A climbing image nudged elastic band method for finding saddle points and minimum energy paths, *J. Chem. Phys.* 113 (22) (2000) 9901–9904, <https://doi.org/10.1063/1.1329672>.
- [38] I.V. Pushkareva, A.S. Pushkarev, V.N. Kalinichenko, R.G. Chumakov, M. A. Soloviev, Y. Liang, P. Millet, S.A. Grigoriev, Reduced graphene oxide-supported Pt-based catalysts for PEM fuel cells with enhanced activity and stability, *Catalysts* 11 (2) (2021) 256, <https://doi.org/10.3390/catal11020256>.
- [39] Y. Zhang, Y.-P. Deng, J. Wang, Y. Jiang, G. Cui, L. Shui, A. Yu, X. Wang, Z. Chen, Recent progress on flexible Zn-air batteries, *Energy Storage Mater.* 35 (2021) 538–549, <https://doi.org/10.1016/j.ensm.2020.09.008>.
- [40] T. Reier, M. Oezaslan, P. Strasser, Electrocatalytic oxygen evolution reaction (OER) on Ru, Ir, and Pt catalysts: a comparative study of nanoparticles and bulk materials, *ACS Catal.* 2 (8) (2012) 1765–1772, <https://doi.org/10.1021/cs3003098>.
- [41] Y. Tang, Y. Li, Z. Yu, Y. Bai, Y. Chen, Y. Sun, P. Wan, Energy-saving synthesis of potassium iodate via electrolysis of potassium iodine and O<sub>2</sub> in a membraneless cell, *Green Chem.* 14 (2) (2012) 334–337, <https://doi.org/10.1039/C2GC16182F>.
- [42] B. Grgur, M. Gvozdenović, J. Stevanović, B. Jugović, L.T. Trisović, Electrochemical oxidation of iodide in aqueous solution, *Chem. Eng. J.* 124 (1–3) (2006) 47–54, <https://doi.org/10.1016/j.cej.2006.08.028>.
- [43] G. Strack, S. Babanova, K.E. Farrington, H.R. Luckarift, P. Atanassov, G.R. Johnson, Enzyme-modified buckypaper for bioelectrocatalysis, *J. Electrochem. Soc.* 160 (7) (2013) G3178, <https://doi.org/10.1149/2.028307jes>.
- [44] W. Liu, C. Ju, D. Jiang, L. Xu, H. Mao, K. Wang, Ionic liquid-assisted grown of beta-nickel hydroxide nanowires on reduced graphene oxide for high-performance supercapacitors, *Electrochim. Acta* 143 (2014) 135–142, <https://doi.org/10.1016/j.electacta.2014.08.010>.
- [45] P. Xu, J. Liu, T. Liu, K. Ye, K. Cheng, J. Yin, D. Cao, G. Wang, Q. Li, Preparation of binder-free CuO/Cu<sub>2</sub>O/Cu composites: a novel electrode material for supercapacitor applications, *RSC Adv.* 6 (34) (2016) 28270–28278, <https://doi.org/10.1039/C6RA00004E>.
- [46] A. Abbasi, S. Hosseini, A. Somwangthanaroj, R. Checharoen, S. Oлару, S. Kheawhom, Discharge profile of a zinc-air flow battery at various electrolyte flow rates and discharge currents, *Sci. Data* 7 (1) (2020) 1–8, <https://doi.org/10.1038/s41597-020-0539-y>.
- [47] N. Logeshwaran, S. Ramakrishnan, S.S. Chandrasekaran, M. Vinothkannan, A. R. Kim, S. Sengodan, D.B. Velusamy, P. Varadhan, J.-H. He, D.J. Yoo, An efficient and durable trifunctional electrocatalyst for zinc-air batteries driven overall water splitting, *Appl. Catal. B Environ.* 297 (2021), 120405, <https://doi.org/10.1016/j.apcatb.2021.120405>.
- [48] T. Sun, J. Wang, C. Qiu, X. Ling, B. Tian, W. Chen, C. Su, B. N codoped and defect-rich nanocarbon material as a metal-free bifunctional electrocatalyst for oxygen reduction and evolution reactions, *Adv. Sci.* 5 (7) (2018) 1800036, <https://doi.org/10.1002/advs.201800036>.
- [49] P. Peng, L. Shi, F. Huo, C. Mi, X. Wu, S. Zhang, Z. Xiang, A pyrolysis-free path toward superiorly catalytic nitrogen-coordinated single atom, *Sci. Adv.* 5 (8) (2019) eaaw2322, <https://doi.org/10.1126/sciadv.aaw2322>.
- [50] J. Wu, H. Zhou, Q. Li, M. Chen, J. Wan, N. Zhang, L. Xiong, S. Li, B.Y. Xia, G. Feng, Densely populated isolated single Co N site for efficient oxygen electrocatalysis, *Adv. Energy Mater.* 9 (22) (2019) 1900149, <https://doi.org/10.1002/aenm.201900149>.
- [51] X. Wang, J. Sunarso, Q. Lu, Z. Zhou, J. Dai, D. Guan, W. Zhou, Z. Shao, High-performance platinum-perovskite composite bifunctional oxygen electrocatalyst for rechargeable Zn-air battery, *Adv. Energy Mater.* 10 (5) (2020) 1903271, <https://doi.org/10.1002/aenm.201903271>.
- [52] X. Han, N. Li, P. Xiong, M.G. Jung, Y. Kang, Q. Dou, Q. Liu, J.Y. Lee, H.S. Park, Electronically coupled layered double hydroxide/MXene quantum dot metallic hybrids for high-performance flexible zinc-air batteries, *InfoMat* 3 (10) (2021) 1134–1144, <https://doi.org/10.1002/inf2.12226>.
- [53] Y. Ling, M. Li, K. Qu, Z. Yang, Electronically interacted Co<sub>3</sub>O<sub>4</sub>/WS<sub>2</sub> as superior oxygen electrode for rechargeable zinc-air batteries, *Chem. Commun.* 56 (96) (2020) 15193–15196, <https://doi.org/10.1039/D0CC07319A>.
- [54] Q. Zhou, Z. Zhang, J. Cai, B. Liu, Y. Zhang, X. Gong, X. Sui, A. Yu, L. Zhao, Z. Wang, Template-guided synthesis of Co nanoparticles embedded in hollow nitrogen doped carbon tubes as a highly efficient catalyst for rechargeable Zn-air batteries, *Nano Energy* 71 (2020), 104592, <https://doi.org/10.1016/j.nanoen.2020.104592>.
- [55] Y. Zhang, H. Qin, M. Alfred, H. Ke, Y. Cai, Q. Wang, F. Huang, B. Liu, P. Lv, Q. Wei, Reaction modifier system enable double-network hydrogel electrolyte for flexible zinc-air batteries with tolerance to extreme cold conditions, *Energy Storage Mater.* 42 (2021) 88–96, <https://doi.org/10.1016/j.ensm.2021.07.026>.
- [56] D. Jiang, H. Wang, S. Wu, X. Sun, J. Li, Flexible zinc-air battery with high energy efficiency and freezing tolerance enabled by DMSO-based organohydrogel electrolyte, *Small Methods* (2021) 2101043, <https://doi.org/10.1002/smtd.202101043>.
- [57] X. Yin, Z. Zhang, K. Yao, X. Xu, Y. Wang, Hydrophobic POM electrocatalyst achieves low voltage “charge” in Zn-air battery coupled with bisphenol A degradation, *Chem. Eur. J.* 27 (34) (2021) 8774–8781, <https://doi.org/10.1002/chem.202100412>.
- [58] X. Zhang, G. Liu, C. Zhao, G. Wang, Y. Zhang, H. Zhang, H. Zhao, Highly efficient electrocatalytic oxidation of urea on a Mn-incorporated Ni(OH)<sub>2</sub>/carbon fiber cloth for energy-saving rechargeable Zn-air batteries, *Chem. Commun.* 53 (77) (2017) 10711–10714, <https://doi.org/10.1039/C7CC04368F>.
- [59] Z. Song, J. Ding, B. Liu, Y. Shen, J. Liu, X. Han, Y. Deng, C. Zhong, W. Hu, Investigation of failure mechanism of rechargeable zinc-air batteries with poly (acrylic acid) alkaline gel electrolyte during discharge-charge cycles at different current densities, *Chem. Eng. J.* 429 (2022), 132331, <https://doi.org/10.1016/j.cej.2021.132331>.
- [60] Z.-B. Wang, P.-J. Zuo, Y.-Y. Chu, Y.-Y. Shao, G.-P. Yin, Durability studies on performance degradation of Pt/C catalysts of proton exchange membrane fuel cell, *Int. J. Hydrog. Energy* 34 (10) (2009) 4387–4394, <https://doi.org/10.1016/j.ijhydene.2009.03.045>.
- [61] J. Wang, G. Yin, Y. Shao, S. Zhang, Z. Wang, Y. Gao, Effect of carbon black support corrosion on the durability of Pt/C catalyst, *J. Power Sources* 171 (2) (2007) 331–339, <https://doi.org/10.1016/j.jpowsour.2007.06.084>.
- [62] K. Jurkiewicz, M. Pawlyta, A. Burian, Structure of carbon materials explored by local transmission electron microscopy and global powder diffraction probes, *C* 4 (4) (2018) 68, <https://doi.org/10.3390/c4040068>.
- [63] M.S. Wilson, F.H. Garzon, K.E. Sickafus, S. Gottesfeld, Surface area loss of supported platinum in polymer electrolyte fuel cells, *J. Electrochem. Soc.* 140 (10) (1993) 2872, <https://doi.org/10.1149/1.2220925>.
- [64] Z. Liu, J. Zhang, P. Yu, J. Zhang, R. Makharia, K. More, E. Stach, Transmission electron microscopy observation of corrosion behaviors of platinumized carbon blacks under thermal and electrochemical conditions, *J. Electrochem. Soc.* 157 (6) (2010) B906, <https://doi.org/10.1149/1.3391737>.
- [65] L. Cao, G. Zhang, S. Jiang, X. Tang, X. Qin, X. Guo, Z. Shao, B. Yi, Enhancing the oxygen reduction reaction performance by modifying the surface of platinum nanoparticles, *ChemElectroChem* 3 (2) (2016) 309–317, <https://doi.org/10.1002/celec.201500387>.